ISSN 0915-633X

NATIONAL INSTITUTE FOR FUSION SCIENCE

Active Trajectory Control for a Heavy Ion Beam Probe on the Compact Helical System

A. Fujisawa, H. Iguchi, S. Lee, T.P. Crowley, Y. Hamada, S. Hidekuma and M. Kojima

(Received - Apr. 5, 1996)

NIFS-415 May 1996

RESEARCH REPORT
NIFS Series

NAGOYA, JAPAN

Active Trajectory Control for A Heavy Ion Beam Probe on the Compact Helical System

A. Fujisawa, H. Iguchi, S. Lee, T. P. Crowley [1], Y. Hamada
S. Hidekuma, M. Kojima

National Institute for Fusion Science,
Furo-cho. Chikusa-ku, Nagoya, 464-01, Japan

Abstract

A 200keV heavy ion beam probe (HIBP) on the Compact Helical System torsatron/heliotron uses a newly proposed method [Review of Scientific Instruments **63** 3694(1992)] in order to control complicated beam trajectories in non-axisymmetrical devices. As a result, the HIBP has successfully measured potential profiles of the toroidal helical plasma. The article will describe the results of the potential profile measurements, together with the HIBP hardware system and procedures to realize the method.

Keywords: Heavy ion beam probe, Active trajectory control, Non-axisymmetrical plasma, Potential Profile Measurements

[1] Rensselaer Polytechnic Institute, Troy, New York, U. S. A.

I. Introduction

The heavy ion beam probe (HIBP) is a unique diagnostic to obtain the information of potential and electron density of plasma interior [2-8] where the electron temperature and density are too high to insert traditional probes. Plasma potential is an important physics quantity for a non-axisymmetric system, such as a torsatron, bumpy torus, since it is associated with plasma confinement and heating efficiency. However, a non-axisymmetrical magnetic field provides a difficult environment for application of HIBPs owing to 3-D beam trajectories[9-11].

An active trajectory control method was proposed for an HIBP of the Compact Helical System (CHS) heliotron/torsatron in order to manage the complicated trajectories[1]. A set of differential equations was found for this method as a conceptual principle to determine sweep voltages to control probing beams for any observation points. A technically essential point to realize this method is an introduction of a secondary beam sweep system in addition to the primary sweep. This scheme gives the following advantages; (1) reducing the potential measurement error caused by uncertainty of beam injection angle into the energy analyzer, (2) expanding the applicable configurations and the observation regions, (3) keeping the energy analyzer away from locations where the magnetic field will disturb the determination of the beam energy.

A 200keV HIBP has been constructed on the CHS, and we have recently obtained potential profiles of rather low density ($\bar{n}_e < 1 \times 10^{13}\mathrm{cm}^{-3}$) plasmas. In this article, we will describe the HIBP system and essential components for the active trajectory control method, and we will present experimental results of potential profile measurements.

II. Principle of Active Trajectory Control

A theoretical guiding principle is given to predict a precise trajectory for the active control[1]. Probing beam trajectories are uniquely determined by beam energy K_0, sweep voltages V_i, and a parameter indicating an ionization point on primary beam trajectory ρ. Infinitesimal changes of these parameters produce corresponding changes in the observation point, the secondary beam position and injection angle at the entrance slit of the energy analyzer, and

other beam parameters of concern. The situation is expressed simply as

$$\Delta\Xi_j = \sum_i \frac{\partial \Xi}{\partial V_i}\Delta V_i + \frac{\partial \Xi}{\partial K_0}\Delta K_0 + \frac{\partial \Xi}{\partial \rho}\Delta\rho\ , \qquad (1)$$

where V_i are the sweep voltages. and Ξ_j represents trajectory parameters; the radial coordinate of ionization point $R_{\rm ion}$, the secondary beam positions and injection angles on the entrance slit $X_{\rm slit}$, $Y_{\rm slit}$, $\theta_{\rm slit}$ and $\varphi_{\rm slit}$, and so on.

If four sweep voltages are provided, the four parameters $X_{\rm slit}$, $Y_{\rm slit}$, $\theta_{\rm slit}$ and $\varphi_{\rm slit}$ can be kept constant during a radial scan with a fixed beam energy. By substituting the condition $\Delta X_{\rm slit} = \Delta Y_{\rm slit} = \Delta\theta_{\rm slit} = \Delta\varphi_{\rm slit} = 0$, Eq. (1) in the matrix form can describe the condition as follows,

$$\begin{pmatrix} \frac{dV_1}{d\rho} \\ \frac{dV_2}{d\rho} \\ \frac{dV_3}{d\rho} \\ \frac{dV_4}{d\rho} \end{pmatrix} = - \begin{pmatrix} \frac{\partial X}{\partial V_1} & \frac{\partial X}{\partial V_2} & \frac{\partial X}{\partial V_3} & \frac{\partial X}{\partial V_4} \\ \frac{\partial Y}{\partial V_1} & \frac{\partial Y}{\partial V_2} & \frac{\partial Y}{\partial V_3} & \frac{\partial Y}{\partial V_4} \\ \frac{\partial \theta}{\partial V_1} & \frac{\partial \theta}{\partial V_2} & \frac{\partial \theta}{\partial V_3} & \frac{\partial \theta}{\partial V_4} \\ \frac{\partial \varphi}{\partial V_1} & \frac{\partial \varphi}{\partial V_2} & \frac{\partial \varphi}{\partial V_3} & \frac{\partial \varphi}{\partial V_4} \end{pmatrix}^{-1} \begin{pmatrix} \frac{\partial X}{\partial \rho} \\ \frac{\partial Y}{\partial \rho} \\ \frac{\partial \theta}{\partial \rho} \\ \frac{\partial \varphi}{\partial \rho} \end{pmatrix} . \qquad (2)$$

After finding a initial beam trajectory parameter set K_0, V_i $(i = 1, 2, 3, 4)$ and ρ (a reference beam trajectory), integration of Eq. (2) yields sweep voltage combinations whose corresponding trajectories pass at an entrance slit point with a proper angle. If the reference beam trajectory is chosen excellently, the obtained set of trajectories may have ionization points covering all over the magnetic flux surface. It has also been proven using Eq. (1) that an observation point is uniquely determined when the sweep voltages V_i $(i = 1, 2, 3, 4)$ and the beam energy K_0 are given.

III. Experimental Set-up for Active Control

III-1. Compact Helical System

The major and average minor radii of the CHS are R =1.0m and $\bar{a}$ =0.20 m, respectively. A pair of helical winding coils and four pairs of poloidal coils are equipped with the CHS for controlling the magnetic field axis and the configuration. The poloidal and toroidal period numbers of the CHS are

$l = 2$ and $m = 8$, respectively. In the CHS, magnetic field configurations are identified by the magnetic axis position R_{ax}.

III-2. Observation Points

In the HIBP system, the primary beam is injected into plasma through the top port, and the secondary beam comes out from the plasma through the horizontal port which is toroidally away from the injection port by τ_{tor} =22.5°. A schematic view of the HIBP system is shown in Fig. 1.

For the magnetic field configuration whose axis and field strength are R_{ax} = 94.9cm and $B_0 = 1$T, respectively, the beam parameters needed to observe the magnetic axis are K_0 =74kV, $V_1 = -568$ V, $V_2 = -507$ V, $V_3 = 120$ V and $V_4 = -36$ V when a cesium beam is used. By integrating Eq. (2) with the above parameters as an initial condition, we can obtain the observation point line shown in Fig. 2a. In this calculation the parameter ρ is chosen to be the vertical coordinate of the ionization position Z_{ion}.

The actual observation points are distributed along the toroidal direction, and the points shown in the figure are the projections obtained by tracing the magnetic field line from the actual observation points. The toroidal angle τ_{tor} of the actual observation points is also shown in Fig. 2b, where $\tau_{tor} = 0$ corresponds to the center of the beam injection top port where the magnetic flux surface is vertically elongated as shown in Fig. 2a. The corresponding sweep voltages combination is also demonstated in Fig. 2c; (V_1, V_2) and (V_3, V_4) represent the voltages of the octupole sweeper on the injection and analyzer sides, respectively.

Figure 3 shows the observation points for the magnetic field configuration whose axis and field strength are R_{ax} = 92.1cm and $B_0 = 1$T, respectively. The beam parameters to observe the magnetic axis are K_0 =88kV, $V_1 = -150$ V, $V_2 = 1397$ V, $V_3 = 400$ V and $V_4 = 88$ V when a cesium beam is used.

III-3. Beam Sweeping System

A wide opening is required for the secondary beam sweep system in order to obtain secondary beams coming from birth points which are widely distributed in plasma. For this purpose, we choose an octupole deflector, in which four

extra plates are used to keep the electric field uniform across most of its wide opening. The conceptual view is illustrated in Fig. 4. In the octupole system, the plates are made of aluminum, and the width and length of each plate and 4.5 cm and 40 cm, respectively. The distance between plates facing each other $d_{\rm oct}$ is 14 cm.

When the voltages of the plates satisfy the following relation

$$\begin{aligned} V_1^{\rm oct} &= -V_5^{\rm oct} = V_x, \\ V_2^{\rm oct} &= -V_6^{\rm oct} = (V_x + V_y)/\sqrt{2}, \\ V_3^{\rm oct} &= -V_7^{\rm oct} = V_y, \\ V_4^{\rm oct} &= -V_8^{\rm oct} = -(V_x - V_y)/\sqrt{2}. \end{aligned} \tag{3}$$

the octupole generates a widely uniform electric field $E_{\rm x} \simeq 2V_{\rm x}/d_{\rm oct}$, $E_{\rm y} \simeq 2V_{\rm y}/d_{\rm oct}$. Note that the primary sweep voltages V_1, V_2, or the secondary sweep voltages V_3, V_4 corresponds to the above defined voltages $V_{\rm x}$, $V_{\rm y}$, respectively. Figure 4 also demonstrates the potential inside the octupole calculated using the Boundary Elemental Method (BEM) when $V_x = 0$ V and $V_y = 1$ V. The electric field is used in the trajectory calculations. The electric field can be regarded as being uniform in the region where the distance from the center is $r < r_0 \sim 4.5$cm.

A high voltage amplifier (Trek 609A-3) is used as a power supply for each plate of the octupoles to realize a high repetition rate for potential profile measurements. The gain and slew rate of the high voltage amplifier are 1000 and $30{\rm V}/\mu s$, respectively. The maximum current capacity of the amplifier is 2mA.

The control system of the sweep voltages should be programmable since the combination of voltages are not composed of simple functions such as a sinusoids, triangular or square waves as was already shown in Figs. 2 and 3. We use a programmable Digital Analog Converter (DAC, Kinetic 3115), which has 4kByte of memory for each channel, to make any function forms. The output signals from the DAC are led into the amplifier inputs, and then the desirable high voltages are produced from the amplifiers.

III-4. Detectors on Secondary Beam Line

The energy of the secondary beams is measured with a 30° parallel plate energy analyzer[12-15]. Beam energy is indicated by the vertical position of the beam on the detector inside the analyzer. The energy analyzer has a secondary order focusing property for injection angle θ, and a first order focusing property for the injection angle φ. A detector behind the analyzer and in line with the desired injection angle of $\theta = 30°$, $\varphi = 0°$ is used the analyzer to examine whether the injection angle is correct. Figure 5 shows the schematic view of the analyzer, and the definition of the injection angles θ, φ.

The split plate detector is used as a detector of the energy analyzer since the detector has a sufficient sensitivity to the beam movement[14,15]. As shown in Fig. 5d, the split plate detector is composed of four separate metal plates which are separated by gaps of several hundred μm and electrically isolated from each other. Each plate has a rectangular shape whose height and width are 5mm and 30mm, respectively. The beam position on the split plate detector are known from the normalized right-left ξ_{RL} and up-down balances ξ_{UD} whose definitions are

$$\xi_{RL} = \frac{i_R - i_L}{i_R + i_L}, \quad \xi_{UD} = \frac{i_U - i_D}{i_U + i_D}, \tag{4}$$

respectively, where i_R and i_L are the sum of the secondary current on the right and left plates, respectively, and i_U and i_D are the sum of the secondary current on the up and down plates, respectively, With the assumption that the secondary beam density is uniform, the horizontal and vertical displacements can be written as

$$\Delta x = \frac{w}{2}\xi_{RL}, \quad \Delta y = \frac{h}{2}\xi_{UD}, \tag{5}$$

respectively, where w and h are the width and height of the entrance slit of the analyzer, respectively. The present height of the entrance slit is 2mm, and the width can be varied from 0 to 40mm.

IV. Experimental Results

IV-1. Trajectory Confirmation Using Gas Ionization

It is an indispensable procedure to confirm that a calculated voltage combination gives the proper probing beam trajectory. A gas ionization process

is available for this purpose; primary beams are injected into the target magnetic field configuration filled with a gas, and the injected primary beam is the ionized through collisions with neutral particles[16]. The detectable secondary beam current is small since the ionization cross sections are smaller compared to those with the plasma, and the charge transfer from neutral gas particles to the beam particles is also a dominant process. If the beam trajectory is controlled properly, the produced secondary beams enter into the energy analyzer with constant up-down ξ_{UD} and right-left ξ_{RL} balances during the radial scans. Particularly, to keep the up-down balance constant is quite important since the parameter ξ_{UD} is directly related to the potential measurements.

Before a calibration using the gas ionization, the primary beam injection angle was checked without magnetic field with a set of wires located about 40cm away from the octupole deflector on the injection side. The primary beam orbit with the magnetic field was also confirmed with a movable detector located on the magnetic axis. Both experiments showed that the primary beam line was in a good agreement with the assumption of the trajectory calculation.

Figure 6 shows (a) time evolutions of the sweep voltages (b) the total secondary intensity with the vertical position of the observation points Z_{ion} and (c) normalized right-left balance ξ_{RL}, and normalized up-down balance ξ_{UD} during radial scanning, for the case of the magnetic configuration whose axis location is R_{ax} =94.9 cm. The amplifier gain for secondary current detection was 0.1V/nA. If a plasma were present, the voltage combinations at $t = 0$ and $t = 100$ms would correspond to its lower and upper edges. The total secondary intensity becomes larger as the ionization point moves toward the upper edge. This can be ascribed to the beam attenuation and the sample volume size difference. Trajectory calculations show that the sample volume size is larger at the upper edge than the lower edge. The secondary trajectories were also checked using the secondary beam detector set behind the analyzer along a $\theta = 30°$ line. The same sweep voltages were used but the analyzer voltage was grounded. This experiment confirmed that the secondary beam entered into the energy analyzer at the proper angle of $\theta = 30°$, $\varphi = 0°$.

Figure 7 shows another example of the gas calibration experiments for the target magnetic field with magnetic field axis location of R_{ax} =92.1 cm. The

tends are similar to the previous case. The voltage combination at $t = 0$ corresponds to the lower edge of the plasma, and the ionization points moves toward the upper edge with an increase of time. The rapid decrease around the upper edge can be ascribed to the beam being scraped off. In both cases, the up-down balance is kept sufficiently constant during the radial scan. The right-left (horizontal) balance is also kept nearly constant during the radial scan.

In these gas calibration experiments the horizontal width of entrance slit is chosen to be 4cm in order to obtain a sufficient secondary beam intensity. According to the trajectory calculation, the sample volumes become larger as the entrance slit widens, and therefore, it may no longer be assumed that the secondary beam density is uniform on the split plate detector in the horizontal direction. Hence, an accurate horizontal beam position can not be estimated from the right-left balance in the gas ionization experiments.

IV-2. Measurements of Potential Profiles

Measurements of potential profiles were performed in electron cyclotron (ECH) and neutral beam injection (NBI) heated plasmas with low electron density of $\bar{n}_e < 1 \times 10^{13}\text{cm}^{-3}$. Here we will present a potential profile in a low density NBI plasma with a magnetic field axis position and magnetic field strength of R_{ax} =92.1cm and 0.9T, respectively. For these conditions, the necessary beam energy is 72keV.

Figure 8 shows results of profile measurements in an NBI heated plasma; (a) the total secondary signal and the average radius of the ionization point at which the secondary is produced, and (b) the normalized right-left balance ξ_{RL} and the normalized up-down balance ξ_{UD}. The current amplifier gain was 0.01V/nA. The average radius of the outermost magnetic surface is 0.19 m for this plasma. A full scan of potential profiles takes about 4ms in this case. The entrance slit was chosen to be 1.4cm in order to reduce the sample volume size. The change of right-left balance is larger than in the gas ionization experiments, but it still has a negligible effect on the potential measurement as will be shown in the discussion. The total secondary intensity signal goes to zero around the plasma edges on the upper and lower edges. This also confirms

the validity of the trajectory control. Note that the upper side may have beam scraped-off, as was seen in the gas ionization experiments. Here the up-down signal shows that the potential is negative.

The absolute value of the space potential is determined from the up-down balance from

$$\phi = 2V_{\rm P}[F(\theta,\ \varphi)\xi_{\rm UD} + G(\theta,\ \varphi)] - V_{\rm A} = \phi_0 + \phi_{\rm offset} + \phi_{\rm corr}, \qquad (6)$$

where $V_{\rm P}$ and $V_{\rm A}$ are the parallel plate voltage and accelerator voltage, respectively, and F and G are the characteristic functions of the analyzer. The three terms are defined as

$$\begin{aligned} \phi_0 &= 2V_{\rm p}F(30^\circ,\ 0^\circ)\xi_{\rm UD} \\ \phi_{\rm offset} &= 2V_{\rm p}G(30^\circ,\ 0^\circ) - V_{\rm A} \\ \phi_{\rm corr} &= 2V_{\rm p}[\Delta F(\Delta\theta,\ \Delta\varphi)\xi_{\rm UD} + \Delta G(\Delta\theta,\ \Delta\varphi)]\ . \end{aligned} \qquad (7)$$

The terms ϕ_0, $\phi_{\rm offset}$, and $\phi_{\rm corr}$ represent the relative change of potential, the offset due to the balance between accelerator and electrode voltages, and the correction owing to the change of the injection angles, respectively.

Accuracy of the offset $\phi_{\rm offset}$ depends on the precision of the function $G(30^\circ,\ 0^\circ)$ and the measurement of the high voltages $V_{\rm P}$ and $V_{\rm A}$. A small uncertainty in the high voltage values results in a large error in the absolute value of the potential. However, the relative potential $\phi_0 = 2V_{\rm p}F(30^\circ,\ 0^\circ)\xi_{\rm UD}$ in Eq. (7) can be estimated with sufficient precision. For the case of $K_0(= V_{\rm A}) = 72$ keV, the potential is estimated as $\phi_0 \simeq 440\xi_{\rm UD}$ since a calibration before installation gave $F(30^\circ,\ 0^\circ) \simeq 1.5 \times 10^{-2}$, $G(30^\circ,\ 0^\circ) \simeq 2.45$[14]. Therefore, using $\xi_{\rm UD}(0) \simeq -0.4$, the potential on the magnetic field axis is about $\phi_0(0) \simeq -200$V. Note that the observation point at the lower edge is located inside of the outermost magnetic surface, as is known from Fig. 3a. That is the reason why the total secondary signal at the point is not completely zero.

V. Discussion

V-1. Reduction of Error due to Injection Angle

The third term in Eq. (6) is associated with the measurement error due to the deviation of the beam injection angle. The error should be reduced with the active control used in these experiments. The functions F and G are explicitly written as

$$F(\theta,\ \varphi) = \frac{h\sin(\theta+\theta_{\rm d})}{4d\sin 2\theta\sin\theta\cos\varphi}\ ,$$
$$G(\theta,\ \varphi) = \frac{L\tan\theta-\alpha\cos\varphi}{2d\sin 2\theta\tan\theta\cos\varphi}\ , \tag{8}$$

where L, $\alpha(=h_1+h_2)$, d and $\theta_{\rm d}$ represent the horizontal distance between the entrance slit and the split plate detector, the vertical length of drift space, the distance between electrodes and the angle of detector surface inclination to the horizontal direction (see Fig. 5). respectively; L = 496.1mm, α = 98.9mm, d = 75.0mm and $\theta_{\rm d} = 60°$ in the energy analyzer of the CHS HIBP. Expanding the above expression in a Taylor series around $\theta = 30°$, $\varphi = 0°$,

$$\Delta F(\Delta\theta,\ \Delta\varphi) = F(30°,\ 0°)\left(-5\sqrt{3}/3\Delta\theta + 1/2\Delta\varphi^2+\cdots\right)\ ,$$
$$\Delta G(\Delta\theta,\ \Delta\varphi) = G(30°,\ 0°)(3/2\Delta\varphi^2+\cdots)\ , \tag{9}$$

where $\Delta\theta = \theta - 30°$, $\Delta\varphi = \varphi$ in radian. By substituting these expressions into Eq. (7), we obtain

$$\phi_{\rm corr} = 2V_{\rm p}\left[F(30°,\ 0°)\xi_{\rm UD}(-5\sqrt{3}/3\Delta\theta+\cdots) + G(30°,\ 0°)(3/2\Delta\varphi^2+\cdots)\right] \tag{10}$$

The injection angle φ can be estimated from the right-left balance parameter $\xi_{\rm RL}$ as $\tan\varphi = w\xi_{\rm RL}/2L$ (see Eq. (5)). The right-left balance $\xi_{\rm RL}$in Fig. 8b is less than 0.5, which gives $\Delta\varphi < 0.5°$ ($\tan\varphi < 7.2\times10^{-3}$). Then Eq. (9) yields $\Delta G/G < 7.8\times10^{-5}$. We can also obtain $\Delta F/F$ <0.02 if $\Delta\theta$ is assumed to be the same as $\Delta\varphi$. For the case of $V_{\rm A}$ = 72keV, $V_{\rm P}$ = 14.7keV, and hence,

$$|\phi_{\rm corr}| < 0.02|\phi_0| + 5.7 < 10 \quad ({\rm V})$$

where we have substituted $|\phi_{0,max}| = 200$V. We conclude, therefore, that in our potential profile measurements the active trajectory control method success-

fully reduced the error caused by the change of the secondary beam injection angles to less than 10V.

V-2. Effects of UV Radiation and Magnetic Field

The active trajectory control method allows the energy analyzer to be moved away from the region where magnetic field and UV radiation from the plasma may disturb normal analyzer operation. As a result, we have never encountered any UV loading or magnetic field problems with the energy analyzer for any plasmas of the CHS.

The octupole deflector, however, is set close to the plasma. In higher density plasmas with NBI ($\bar{n}_e > 1 \times 10^{13}\mathrm{cm}^{-3}$), the secondary beam sweep plates frequently could not hold the proper voltages, probably since the strong radiation from the plasmas induces small arcs. The easiest way to solve the problem is to reinforce the power supply capability.

Actually, the proper voltage could be held when we used another high voltage amplifier (Trek 664) whose slew rate and current capacity are 180 V/μs and 20mA, respectively. Figure 9 shows the monitored voltages on a pair of octupole plates using two different high voltage amplifiers (Trek 664 and Trek 609-A) when the plasma density is about $\bar{n}_e = 6 \times 10^{13}\mathrm{cm}^{-3}$. It is clear that the power supply with high performance can hold the voltage well while the other loses control of the voltage.

The monitored current for the Trek 664 is also shown in Fig. 9b, together with a radiation signal measured with a pyrometer. The observed spiky current flow is considered to be induced according to small arcs when the plasma UV radiation is strong. Thus, high slew rate and large current capacity will be important, and it is also expected that improvement of the octupole structure may reduce the necessary slew rate and current capacity.

In conclusion, the active trajectory control method works successfully for HIBPs such as one on the CHS torsatron/heliotron, giving the following advantages; (i) reduction of the error caused by uncertainty of the injection angle of the beam, (ii) extension of observable range, (iii) reduction of magnetic field disturbances on the energy analyzer. The method will be applicable for other plasmas.

Acknowledgements

We would like to thank Dr. A. Nishizawa for our use of his beam profile moniter. We are also grateful to Dr. K. Matsuoka, Dr. S. Okamura and the CHS experimental group for their cooperation.

References

1) A. Fujisawa, H. Iguchi, M. Sasao, Y. Hamada, J. Fujita, Rev. Sci. Instrum. **63** 3694(1992).

2) F. C. Jobes and R. L. Hickok, Nucl. Fusion, **10**, 195(1970).

3) J. C. Hosea, F. C. Jobes, R. L. Hickok and A. N. Dillis, Phys. Rev. Lett. **30**, 839(1973).

4) F. M. Bieniosek, P. L. Colestock, K. A. Connor, R. L. Hickok. S. P. Kuo, R. A. Dandl, Rev. Sci. Instrum. **51**, 206(1980).

5) K. Takasugi, H. Iguchi, M. Fujiwara, H. Ikegami, Jpn. J. Appl. Phys. **23**, 364(1984).

6) P. M. Schoch, J. C. Forster, W. C. Jennings and R. L. Hickok, Rev. Sci. Intrum. **57**, 1825(1986).

7) R. L. Hickok and P. M. Schoch, Rev. Sci. Intrum. **59**, 1685(1988).

8) G. A. Hallock, J. Mathew, W. C. Jennings, and R. L. Hickok, Phys. Rev. Lett. **56**, 1248(1986).

9) J. J. Zielinski, S. C. Aceto, K. A. Connor et al., Rev. Sci. Instrum. **61**, 2961(1990).

10) A. Carnevali, K. A. Connor, S. C. Aceto, et al., Rev. Sci. Instrum. **59**, 1670(1988).

11) A. Carnevali, J. R. Misium, J. F. Lewis, and K. A. Connor, Rev. Sci. Instrum. **57**, 1822(1986).

12) T. S. Green and G. A. Proca, Rev. Sci. Instrum. **41**, 1409(1970).

13) G. A. Proca and T. S. Green, Rev. Sci. Instrum. **41**, 1778(1970).

14) A. Fujisawa, H. Iguchi, Y. Hamada, Rev. Sci. Intrum. **65**, 1580(1994).

15) L. Solensten and K. A. Connor, Rev. Sci.Instrum. **58**, 516(1987).

16) I. Alvare, C. Cisneros, C. F. Barnett and J. A. Ray, Phys. Rev. A **13**, 1728(1976).

Figure Captions

Fig. 1: A conceptual view of the 200 keV heavy ion beam probe on the CHS. The port of the energy analyzer is located away from the injection port by 22.5° in the toroidal direction.

Fig. 2: Observation points for the magnetic field configuration whose axis position is R_{ax} =94.9 cm in the CHS.(a) Location of the observation points on a magnetic flux surface by tracing the magnetic field line (b) the toroidal coordinate of the observation points (c) corresponding sweep voltage combinations.

Fig. 3: Observation points for the magnetic field configuration whose axis position is R_{ax} =92.1 cm in the CHS. (a) Location of the observation points on a magnetic flux surface by tracing the magnetic field line (b) the toroidal coordinate of the observation points (c) corresponding sweep voltage combinations.

Fig. 4: (a) Schematic view of octupole deflector system (b) potential distribution inside the octupole deflectors.

Fig. 5: Beam detection and energy analyzing system. (a) Side view of energy analyzer, (b) top view of energy analyzer, (c) side view of split plate detector, (d) front view of split plate detector.

Fig. 6: Trajectory calibration using gas ionization process for magnetic field configuration whose magnetic axis is R_{ax} =94.9 cm. (a) Sweep voltage time evolution, (b) total secondary beam intensity and the vertical coordinate of the ionization point Z_{ion}, (c) normalized right-left and up-down balances obtained with helium gas ionization.

Fig. 7: Trajectory calibration using gas ionization process for magnetic field configuration whose magnetic axis is 92.1 cm. (a) Sweep voltage time evolution, (b) total secondary beam intensity and the vertical coordinate of the ionization point Z_{ion}, (c) normalized right-left and up-down balances obtained with helium gas ionization.

Fig. 8: An example of the potential profile measurements in a NBI plasma whose magnetic axis is located on R_{ax} =92.1 cm. Time evolutions of (a) total secondary beam intensity with average radius of the observation

point, and (b) normalized right-left balance ξ_{RL} and normalized up-down balance ξ_{UD}.

Fig. 9: (a) Voltages on plates of the octupole deflector using two different high voltage amplifiers (Trek 609-A, Trek 664). The slew rates of the Trek 664 and the Trek 609-A are 180V/μs and 30V/μ, respectively. The current capacity of the Trek 664 and the Trek 609-A are 20mA and 2mA, respectively. (b) Induced current flow moniterd for the Trek 664 (solid line), together with a pyrometer signal (dashed line).

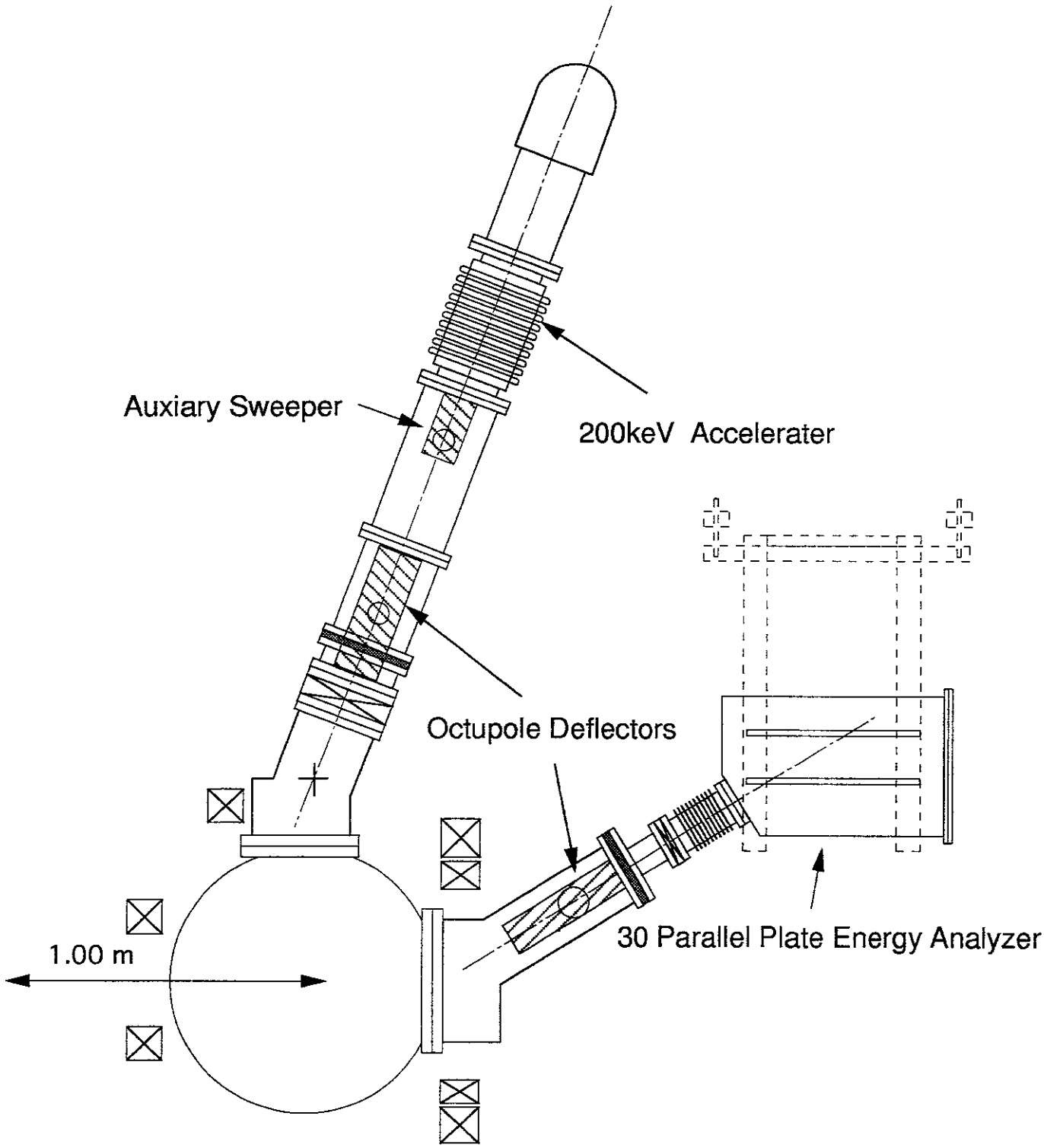
Auxiary Sweeper
200keV Accelerater
Octupole Deflectors
30 Parallel Plate Energy Analyzer
1.00 m

Figure 1

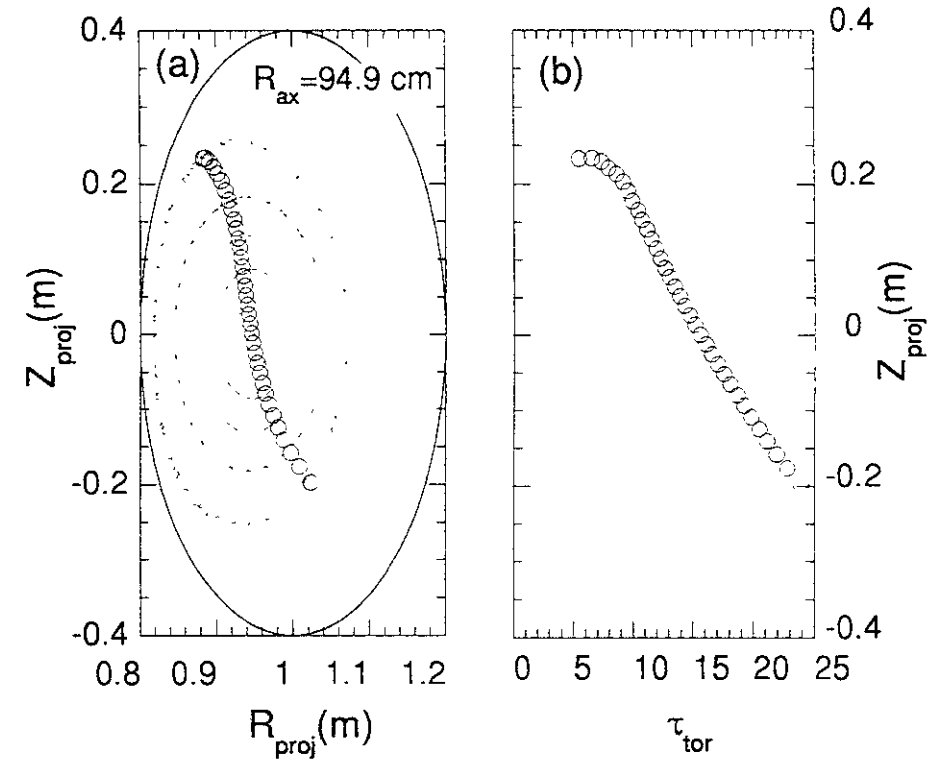
(a)
R_ax=94.9 cm
Z_proj(m)
R_proj(m)
0.4
0.2
0
-0.2
-0.4
0.8
0.9
1
1.1
1.2
(b)
τ_tor
0
5
10
15
20
25

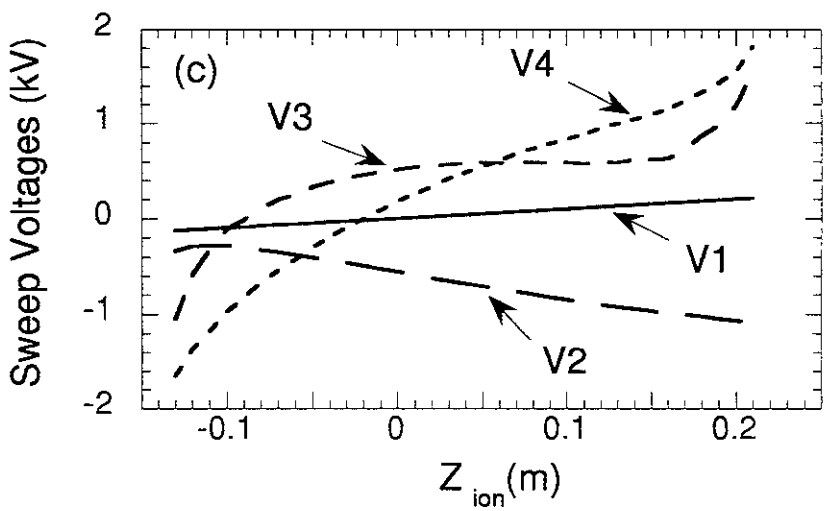
(c)
V4
V3
V1
V2
Sweep Voltages (kV)
Z_ion(m)
2
1
0
-1
-2
-0.1
0
0.1
0.2

Figure 2

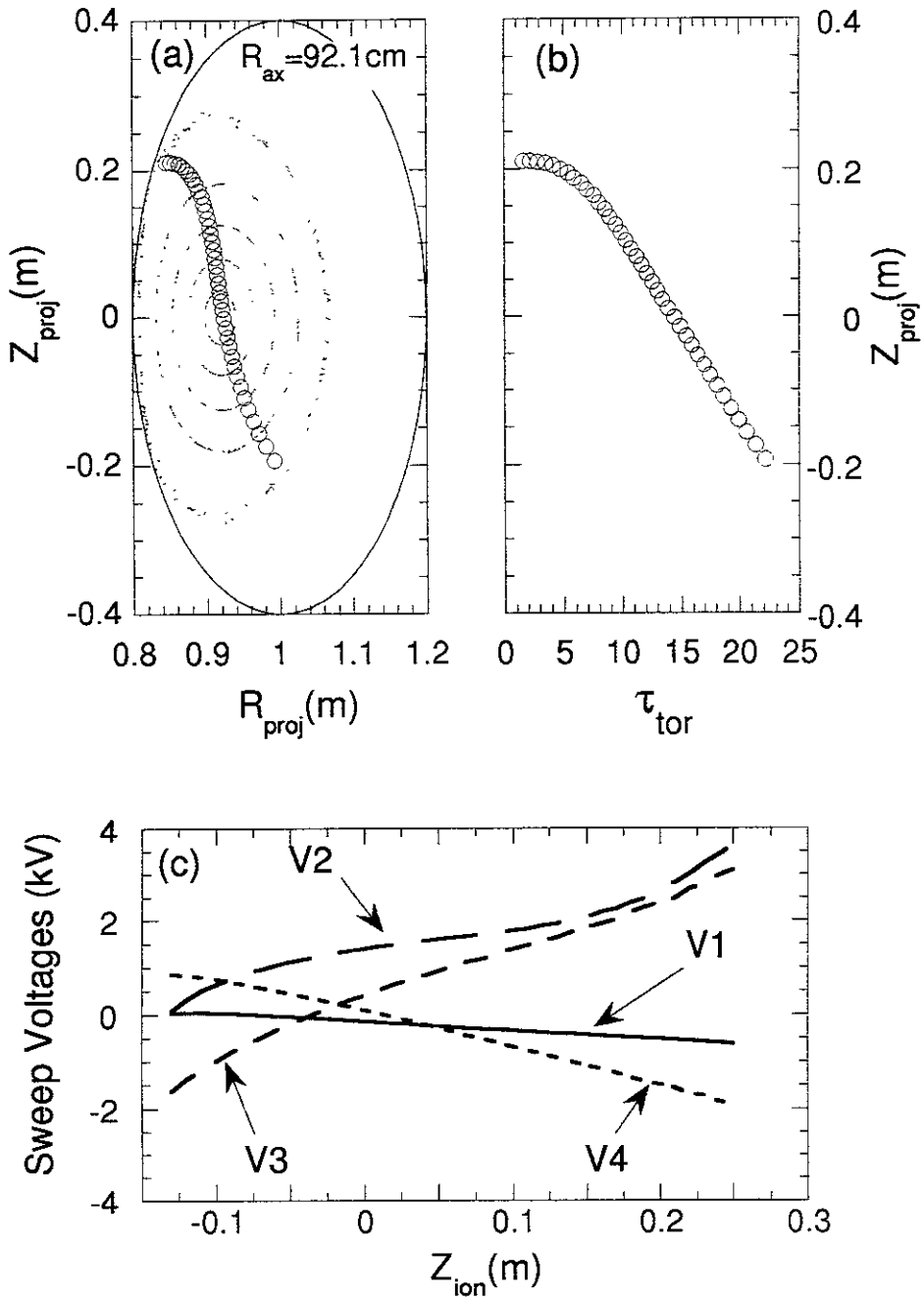
(a)
R_{ax}=92.1cm
(b)
Z_{proj}(m)
R_{proj}(m)
τ_{tor}
(c)
V2
V1
V3
V4
Sweep Voltages (kV)
Z_{ion}(m)

Figure 3

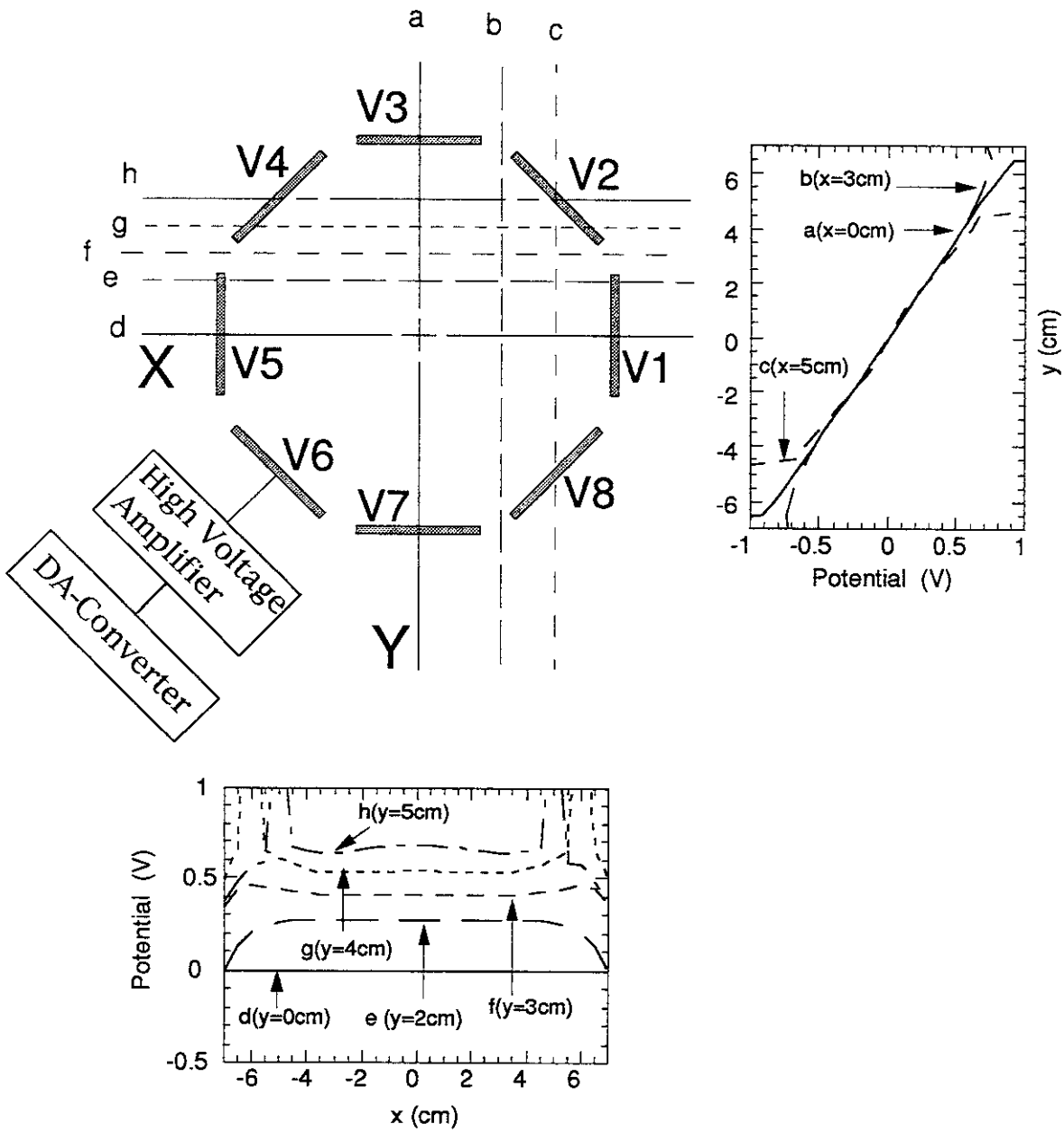
a
b
c
V3
V4
V2
h
g
f
e
d
X
V5
V1
V6
V7
V8
Y
High Voltage Amplifier
DA-Converter
b(x=3cm)
a(x=0cm)
c(x=5cm)
Potential (V)
y (cm)
h(y=5cm)
g(y=4cm)
d(y=0cm)
e (y=2cm)
f(y=3cm)
Potential (V)
x (cm)

Figure 4

a) Side View

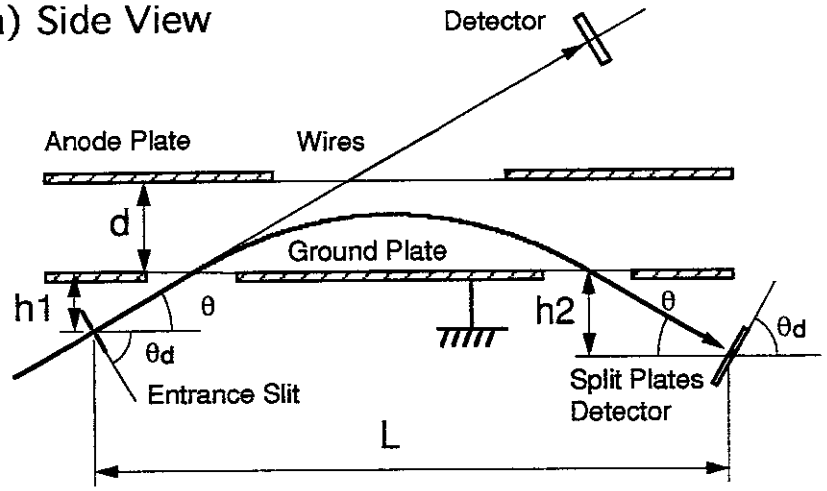

b) Top View

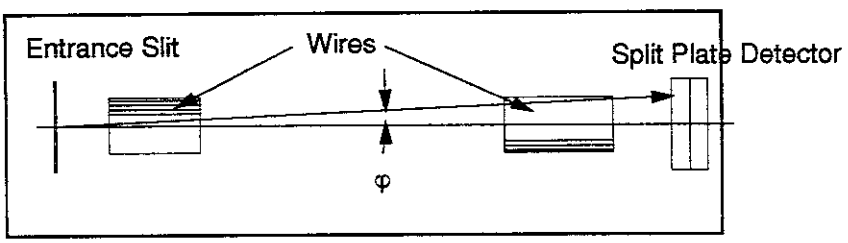

c) Split Plate (side view)

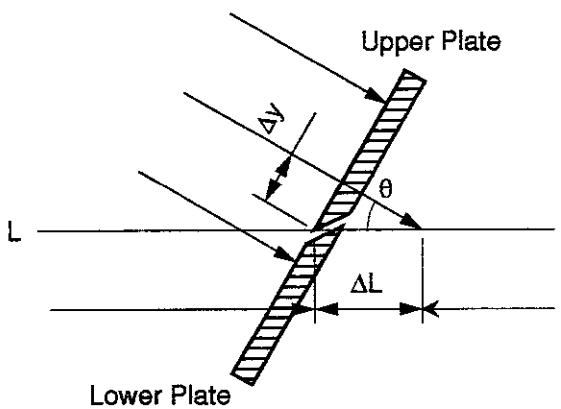

d) Split Plat (front view)

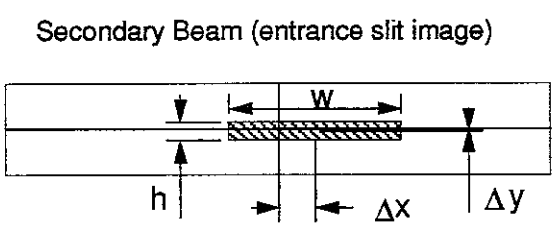

Figure 5

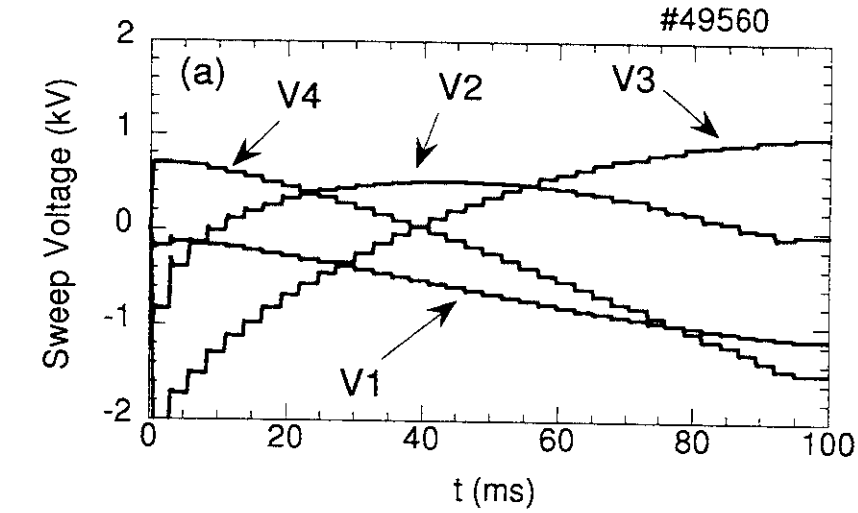
#49560
(a)
V4
V2
V3
V1
Sweep Voltage (kV)
t (ms)

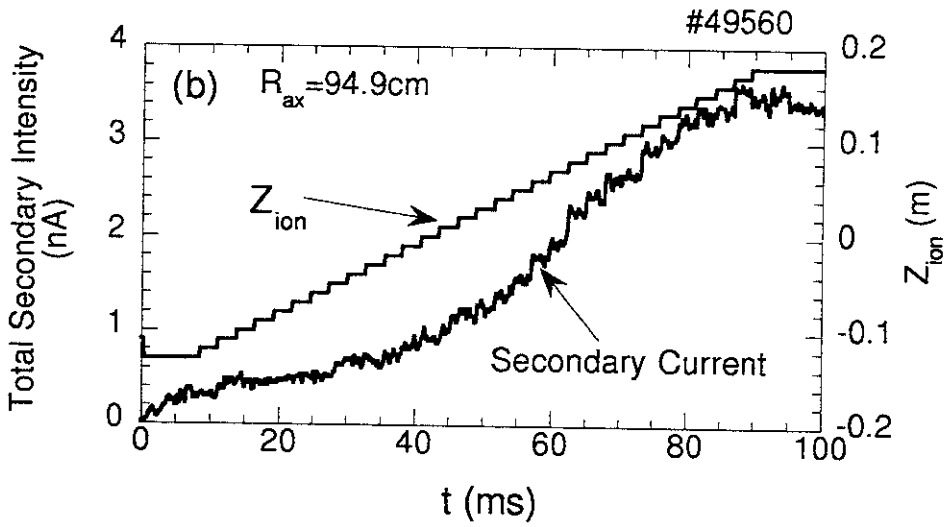
#49560
(b)
R_{ax}=94.9cm
Z_{ion}
Secondary Current
Total Secondary Intensity (nA)
Z_{ion} (m)
t (ms)

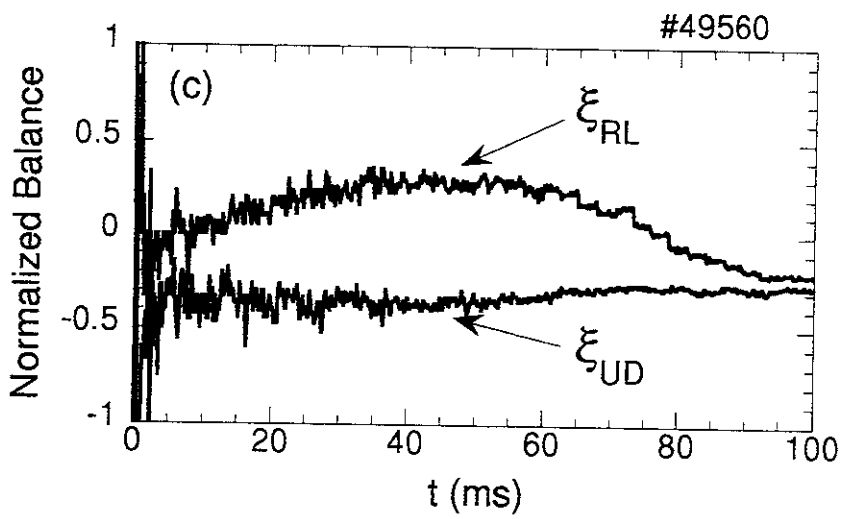
#49560
(c)
ξ_{RL}
ξ_{UD}
Normalized Balance
t (ms)

Figure 6

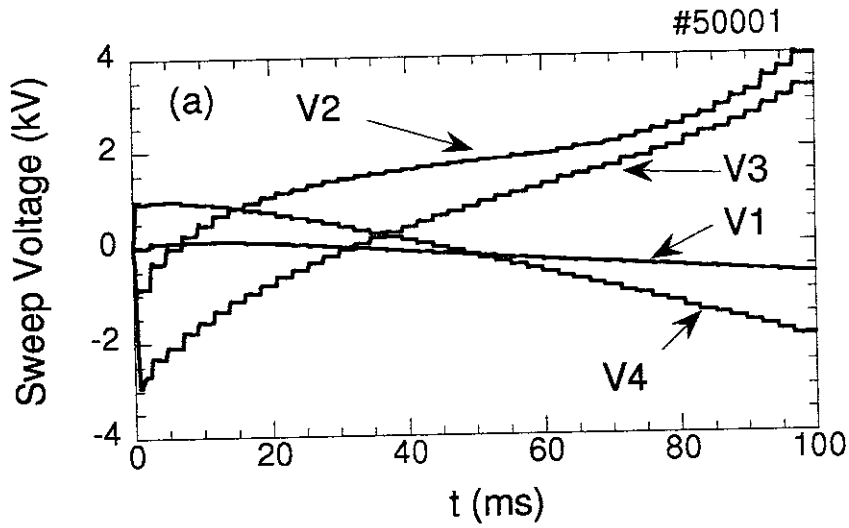
#50001
(a)
V2
V3
V1
V4
Sweep Voltage (kV)
t (ms)

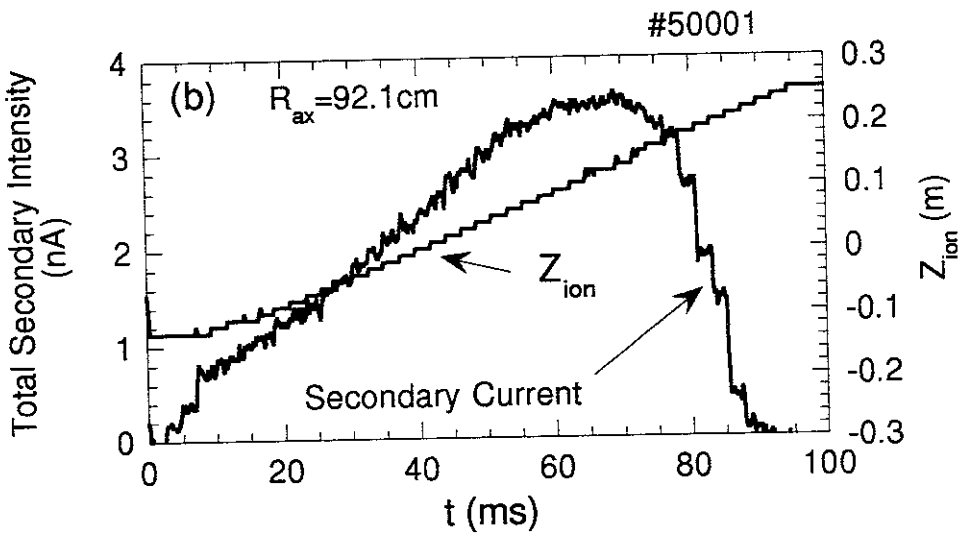
#50001
(b)
R_{ax}=92.1cm
Z_{ion}
Secondary Current
Total Secondary Intensity (nA)
Z_{ion} (m)
t (ms)

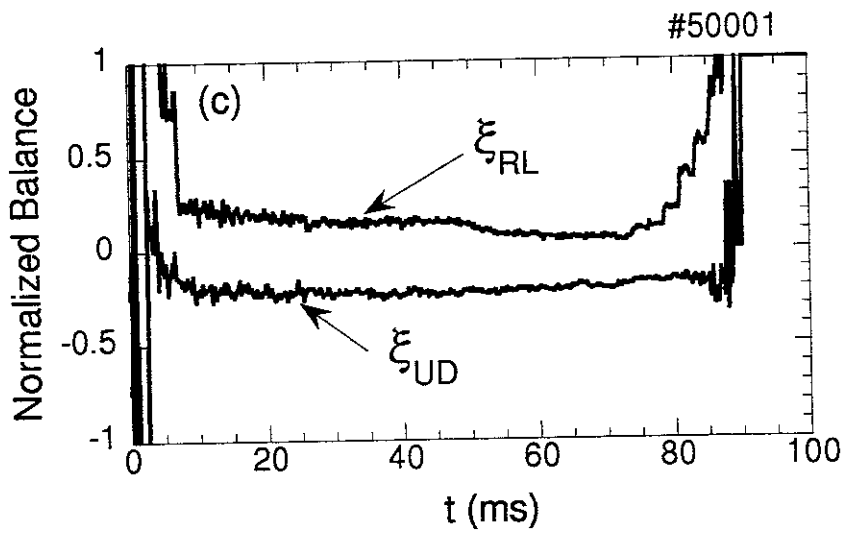
#50001
(c)
ξ_{RL}
ξ_{UD}
Normalized Balance
t (ms)

Figure 7

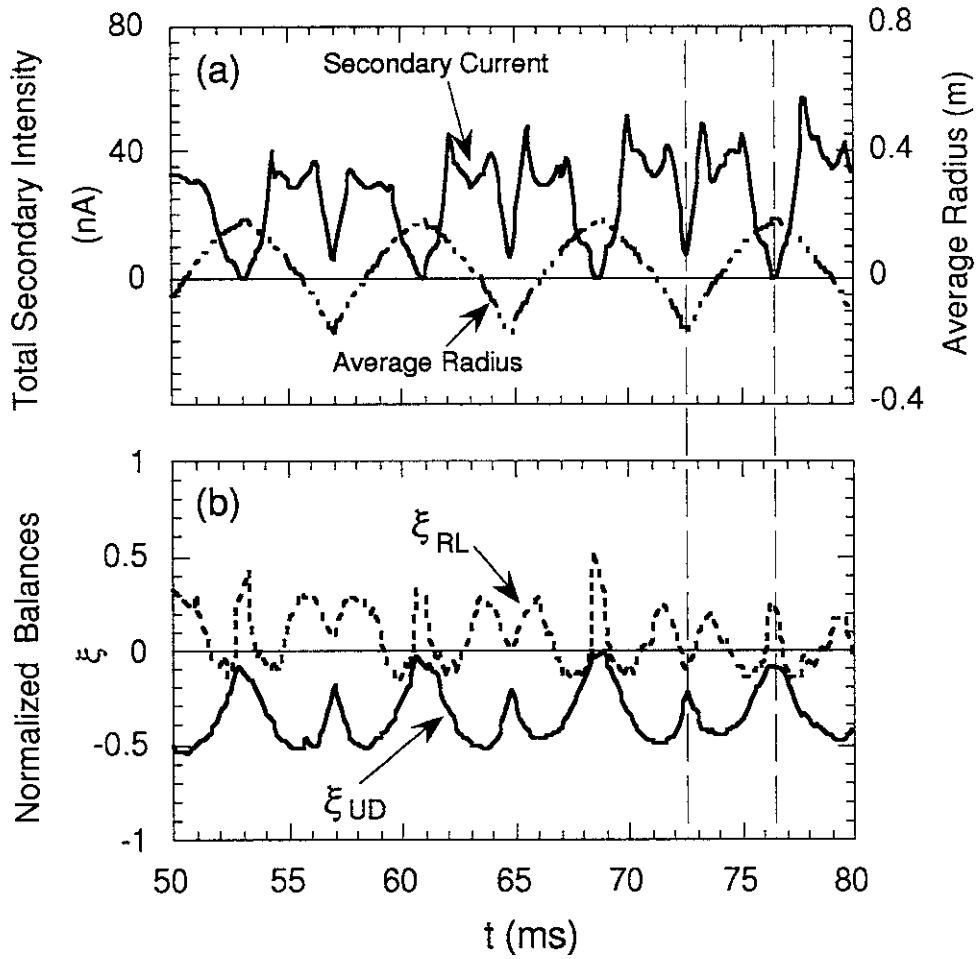
(a)
Secondary Current
Average Radius
Total Secondary Intensity
(nA)
Average Radius (m)
80
40
0
0.8
0.4
0
-0.4
(b)
ξ_{RL}
ξ_{UD}
Normalized Balances
ξ
1
0.5
0
-0.5
-1
50
55
60
65
70
75
80
t (ms)

Figure 8

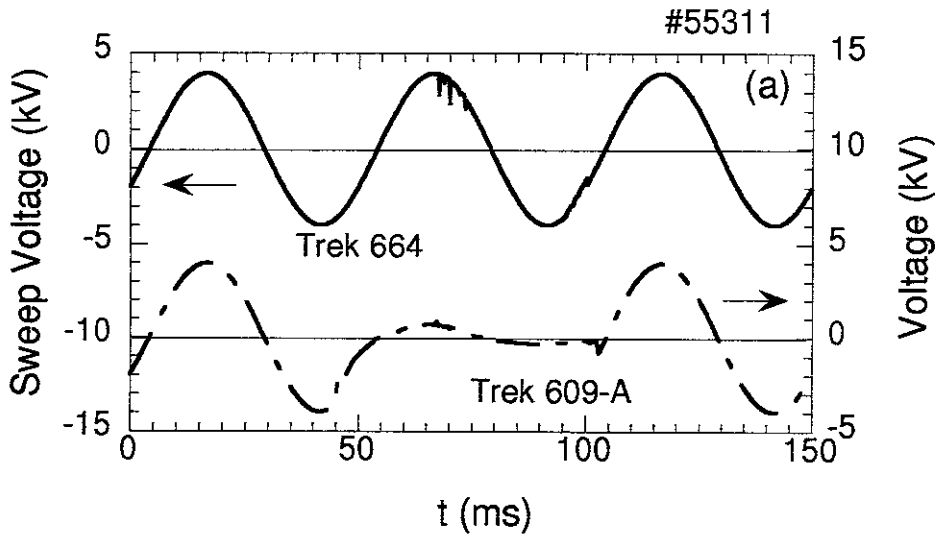
#55311
(a)
Sweep Voltage (kV)
Voltage (kV)
Trek 664
Trek 609-A
t (ms)
5
0
-5
-10
-15
15
10
5
0
-5
0
50
100
150

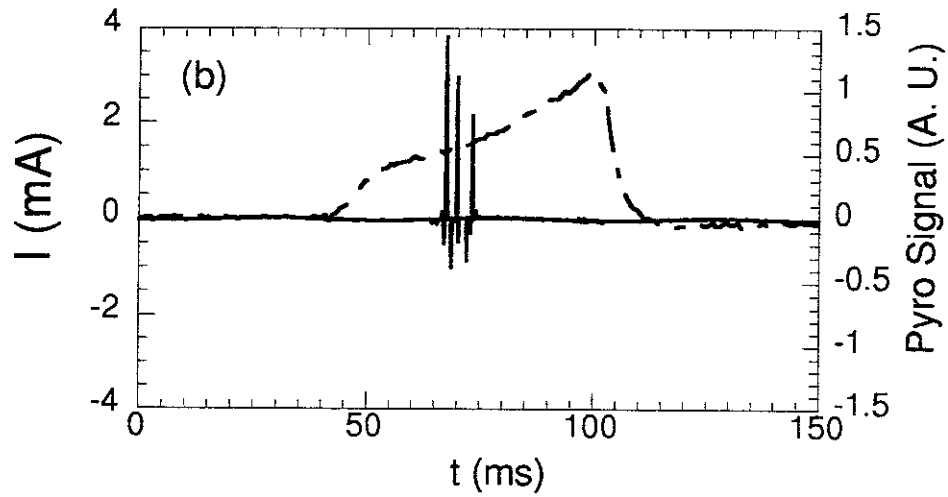
(b)
I (mA)
Pyro Signal (A. U.)
t (ms)
4
2
0
-2
-4
1.5
1
0.5
0
-0.5
-1
-1.5
0
50
100
150

Figure 9

Recent Issues of NIFS Series

NIFS-368 Y. Takeiri, O. Kaneko, Y. Oka, K. Tsumori, E. Asano, R. Akiyama, T. Kawamoto and T. Kuroda,
Multi-Beamlet Focusing of Intense Negative Ion Beams by Aperture Displacement Technique; Aug. 1995

NIFS-369 A. Ando, Y. Takeiri, O. Kaneko, Y. Oka, K. Tsumori, E. Asano, T. Kawamoto, R. Akiyama and T. Kuroda,
Experiments of an Intense H- Ion Beam Acceleration; Aug. 1995

NIFS-370 M. Sasao, A. Taniike, I. Nomura, M. Wada, H. Yamaoka and M. Sato,
Development of Diagnostic Beams for Alpha Particle Measurement on ITER; Aug. 1995

NIFS-371 S. Yamaguchi, J. Yamamoto and O. Motojima;
A New Cable -in conduit Conductor Magnet with Insulated Strands; Sep. 1995

NIFS-372 H. Miura,
Enstrophy Generation in a Shock-Dominated Turbulence; Sep. 1995

NIFS-373 M. Natsir, A. Sagara, K. Tsuzuki, B. Tsuchiya, Y. Hasegawa, O. Motojima,
Control of Discharge Conditions to Reduce Hydrogen Content in Low Z Films Produced with DC Glow; Sep. 1995

NIFS-374 K. Tsuzuki, M. Natsir, N. Inoue, A. Sagara, N. Noda, O. Motojima, T. Mochizuki, I. Fujita, T. Hino and T. Yamashina,
Behavior of Hydrogen Atoms in Boron Films during H_2 and He Glow Discharge and Thermal Desorption; Sep. 1995

NIFS-375 U. Stroth, M. Murakami, R.A. Dory, H. Yamada, S. Okamura, F. Sano and T. Obiki,
Energy Confinement Scaling from the International Stellarator Database; Sep. 1995

NIFS-376 S. Bazdenkov, T. Sato, K. Watanabe and The Complexity Simulation Group,
Multi-Scale Semi-Ideal Magnetohydrodynamics of a Tokamak Plasma; Sep. 1995

NIFS-377 J. Uramoto,
Extraction of Negative Pionlike Particles from a H2 or D2 Gas Discharge Plasma in Magnetic Field; Sep. 1995

NIFS-378 K. Akaishi,
Theoretical Consideration for the Outgassing Characteristics of an Unbaked Vacuum System; Oct. 1995

NIFS-379 H. Shimazu, S. Machida and M. Tanaka,
Macro-Particle Simulation of Collisionless Parallel Shocks; Oct. 1995

NIFS-380 N. Kondo and Y. Kondoh,
Eigenfunction Spectrum Analysis for Self-organization in Dissipative Solitons; Oct. 1995

NIFS-381 Y. Kondoh, M. Yoshizawa, A. Nakano and T. Yabe,
Self-organization of Two-dimensional Incompressible Viscous Flow in a Friction-free Box; Oct. 1995

NIFS-382 Y.N. Nejoh and H. Sanuki,
The Effects of the Beam and Ion Temperatures on Ion-Acoustic Waves in an Electron Beam-Plasma System; Oct. 1995

NIFS-383 K. Ichiguchi, O. Motojima, K. Yamazaki, N. Nakajima and M. Okamoto
Flexibility of LHD Configuration with Multi-Layer Helical Coils;
Nov. 1995

NIFS-384 D. Biskamp, E. Schwarz and J.F. Drake,
Two-dimensional Electron Magnetohydrodynamic Turbulence; Nov. 1995

NIFS-385 H. Kitabata, T. Hayashi, T. Sato and Complexity Simulation Group,
Impulsive Nature in Collisional Driven Reconnection; Nov. 1995

NIFS-386 Y. Katoh, T. Muroga, A. Kohyama, R.E. Stoller, C. Namba and O. Motojima,
Rate Theory Modeling of Defect Evolution under Cascade Damage Conditions:The Influence of Vacancy-type Cascade Remnants and Application to the Defect Production Chracterization by Microstructural Analysis; Nov. 1995

NIFS-387 K. Araki, S. Yanase and J. Mizushima,
Symmetry Breaking by Differential Rotation and Saddle-node Bifurcation of the Thermal Convection in a Spherical Shell; Dec. 1995

NIFS-388 V.D. Pustovitov,
Control of Pfirsch-Schlüter Current by External Poloidal Magnetic Field in Conventional Stellarators: Dec. 1995

NIFS-389 K. Akaishi,
On the Outgassing Rate Versus Time Characteristics in the Pump-down of an Unbaked Vacuum System; Dec. 1995

NIFS-390 K.N. Sato, S. Murakami, N. Nakajima, K. Itoh,
Possibility of Simulation Experiments for Fast Particle Physics in Large Helical Device (LHD); Dec. 1995

NIFS-391 W.X.Wang, M. Okamoto, N. Nakajima, S. Murakami and N. Ohyabu,

A Monte Carlo Simulation Model for the Steady-State Plasma in the Scrape-off Layer; Dec. 1995

NIFS-392 Shao-ping Zhu, R. Horiuchi, T. Sato and The Complexity Simulation Group, *Self-organization Process of a Magnetohydrodynamic Plasma in the Presence of Thermal Conduction;* Dec. 1995

NIFS-393 M. Ozaki, T. Sato, R. Horiuchi and the Complexity Simulation Group *Electromagnetic Instability and Anomalous Resistivity in a Magnetic Neutral Sheet*; Dec. 1995

NIFS-394 K. Itoh, S.-I Itoh, M. Yagi and A. Fukuyama, *Subcritical Excitation of Plasma Turbulence*; Jan. 1996

NIFS-395 H. Sugama and M. Okamoto, W. Horton and M. Wakatani, *Transport Processes and Entropy Production in Toroidal Plasmas with Gyrokinetic Eletromagnetic Turbulence;* Jan. 1996

NIFS-396 T. Kato, T. Fujiwara and Y. Hanaoka, *X-ray Spectral Analysis of Yohkoh BCS Data on Sep. 6 1992 Flares - Blue Shift Component and Ion Abundances -;* Feb. 1996

NIFS-397 H. Kuramoto, N. Hiraki, S. Moriyama, K. Toi, K. Sato, K. Narihara, A. Ejiri, T. Seki and JIPP T-IIU Group, *Measurement of the Poloidal Magnetic Field Profile with High Time Resolution Zeeman Polarimeter in the JIPP T-IIU Tokamak*; Feb. 1996

NIFS-398 J.F. Wang, T. Amano, Y. Ogawa, N. Inoue, *Simulation of Burning Plasma Dynamics in ITER*; Feb. 1996

NIFS-399 K. Itoh, S-I. Itoh, A. Fukuyama and M. Yagi, *Theory of Self-Sustained Turbulence in Confined Plasmas*; Feb. 1996

NIFS-400 J. Uramoto, *A Detection Method of Negative Pionlike Particles from a H2 Gas Descharge Plasma*; Feb. 1996

NIFS-401 K.Ida, J.Xu, K.N.Sato, H.Sakakita and JIPP TII-U group, *Fast Charge Exchange Spectroscopy Using a Fabry-Perot Spectrometer in the JIPP TII-U Tokamak;* Feb. 1996

NIFS-402 T. Amano, *Passive Shut-Down of ITER Plasma by Be Evaporation;* Feb. 1996

NIFS-403 K. Orito, A New Variable Transformation Technique for the Nonlinear Drift Vortex; Feb. 1996

NIFS-404 T. Oike, K. Kitachi, S. Ohdachi, K. Toi, S. Sakakibara, S. Morita, T.

Morisaki, H. Suzuki, S. Okamura, K. Matsuoka and CHS group;
Measurement of Magnetic Field Fluctuations near Plasma Edge with Movable Magnetic Probe Array in the CHS Heliotron/Torsatron; Mar. 1996

NIFS-405 S.K. Guharay, K. Tsumori, M. Hamabe, Y. Takeiri, O. Kaneko, T. Kuroda,
Simple Emittance Measurement of H- Beams from a Large Plasma Source; Mar. 1996

NIFS-406 M. Tanaka and D. Biskamp,
Symmetry-Breaking due to Parallel Electron Motion and Resultant Scaling in Collisionless Magnetic Reconnection; Mar. 1996

NIFS-407 K. Kitachi, T. Oike, S. Ohdachi, K. Toi, R. Akiyama, A. Ejiri, Y. Hamada, H.Kuramoto, K. Narihara, T. Seki and JIPP T-IIU Group,
Measurement of Magnetic Field Fluctuations within Last Closed Flux Surface with Movable Magnetic Probe Array in the JIPP T-IIU Tokamak; Mar. 1996

NIFS-408 K. Hirose, S. Saito and Yoshi.H. Ichikawa
Structure of Period-2 Step-1 Accelerator Island in Area Preserving Maps; Mar. 1996

NIFS-409 G.Y.Yu, M. Okamoto, H. Sanuki, T. Amano,
Effect of Plasma Inertia on Vertical Displacement Instability in Tokamaks; Mar. 1996

NIFS-410 T. Yamagishi,
Solution of Initial Value Problem of Gyro-Kinetic Equation; Mar. 1996

NIFS-411 K. Ida and N. Nakajima,
Comparison of Parallel Viscosity with Neoclassical Theory; Apr. 1996

NIFS-412 T. Ohkawa and H. Ohkawa,
Cuspher, A Combined Confinement System; Apr. 1996

NIFS-413 Y. Nomura, Y.H. Ichikawa and A.T. Filippov,
Stochasticity in the Josephson Map; Apr. 1996

NIFS-414 J. Uramoto,
Production Mechanism of Negative Pionlike Particles in H_2 Gas Discharge Plasma; Apr. 1996

NIFS-415 A. Fujisawa, H. Iguchi, S. Lee, T.P. Crowley, Y. Hamada, S. Hidekuma, M. Kojima,
Active Trajectory Control for a Heavy Ion Beam Probe on the Compact Helical System; May 1996